J. Fluid Mech. (2003), *vol.* 492, *pp.* 181–205.
DOI: 10.1017/S002211200300555X Printed in the United Kingdom

Nearly symmetric and nearly baroclinic instabilities in the presence of diffusivity. Part 1. Growth rate patterns

By QIN XU

NOAA National Severe Storms Laboratory, 1313 Halley Circle, Norman, OK 73069, USA
Qin.Xu@nssl.noaa.gov

(Received 6 March 2002 and in revised form 28 April 2003)

Computations are performed to examine the instabilities of baroclinically sheared Eady basic flows with respect to banded normal-mode perturbations in three-dimensional space in the presence of eddy diffusivity with two (free-slip and non-slip) types of boundary conditions. The non-dimensional model system contains four external parameters: the Richardson number, the Ekman number, the Prandtl number and the ratio between inertial and buoyancy frequencies. The solutions are controlled mainly by the first three parameters. Growth rate patterns are computed for unstable modes as functions of the horizontal wavelength, l, and tilt angle α of the band orientation with respect to the basic shear (measured negative clockwise from the basic-shear direction). It is found that the main growth rate pattern (for non-propagating modes with respect to the middle-level basic flow) has only one maximum unless the Ekman number is sufficiently small. The growth rate pattern obtained with the free-slip boundary conditions has a slightly larger global maximum and is more symmetric with respect to the symmetric axis in the (l, α) space than that obtained with the non-slip boundary conditions. When the Richardson number is increased from 0.25 to 1.0, the maximum growth rate decreases and the associated instability changes gradually from a nearly symmetric type to a nearly baroclinic type as manifested by the continuous increase of l (from mesoscale to synoptic scale) and continuous change of α (from nearly zero to nearly $-90°$). When the Ekman number is sufficiently small, the main growth rate pattern can have two local maxima if the Richardson number is within a subrange $0.8 < Ri < 1.0$. One of the local maxima is near the symmetric axis and the other is near the baroclinic axis in the wavenumber space. When the Richardson number increases through a transitional value in the subrange, the global maximum growth rate decreases continuously but the maximum point jumps from one local maximum to the other and the associated instability switches from a nearly symmetric type to a nearly Eady baroclinic type. The subrange depends on the smallness of the Ekman number and it diminishes as the Ekman number increases to 0.0025 (for the non-slip case). The computed growth rates and (l, α) are compared with the nearly inviscid results of Miller & Antar and the inviscid results of Stone.

1. Introduction

One of the important stability problems in geophysical fluid dynamics, the instabilities of the Eady baroclinic basic state in three-dimensional space, has been studied by Stone (1966, 1970, 1972) and Tokioka (1970). According to Stone (1966,

1970), when the Richardson number is in the range $1 > Ri > 0.84$, the inviscid growth rates have two local maxima in the wavenumber space: one is at the infinite point of the symmetric axis associated with the classic symmetric instability (Fjortoft 1944) and the other is on the baroclinic axis associated with the classic baroclinic instability (Eady 1949). This feature was interpreted as the coexistence of the two types of instability. The global maximum is the baroclinic one if $1 > Ri > 0.95$, and the symmetric one if $0.95 > Ri > 0.84$. Thus, the instability associated with the global maximum point switches from one type to the other when Ri changes through the transitional value of $Ri^* = 0.95$. When the Richardson number becomes smaller than 0.84, the baroclinic local maximum degenerates into a saddle point and, thus, the only maximum is the symmetric one until Ri becomes smaller than $1/4$ and the classic Kelvin–Helmholtz instability becomes dominant. Thus, as summarized by Stone (1970), the largest growth rate is associated with the Kelvin–Helmholtz instability if $1/4 > Ri > 0$, with the symmetric instability if $Ri^* > Ri > 1/4$, and with the baroclinic instability if $Ri > Ri^*$, where $Ri^* = 0.95$ is the transitional Richardson number for the inviscid instabilities.

The destabilization effects of double diffusivities (characterized by non-unity Prandtl number) on the symmetric instability were discovered by McIntyre (1970), who demonstrated the dependence of the critical Richardson number on the Prandtl number even in the limit when the diffusivities approach zero; that is, the critical Richardson number becomes gradually higher than the classic value (that is, $Ri = 1$ for inviscid symmetric instability) as the Prandtl number moves away from unity. By relaxing the symmetric constraint and allowing the perturbation bands to have a small horizontal angle with respect to the basic shear, the analysis of Busse & Chen (1981) indicated that in the presence of double diffusivities the maximum critical Richardson number occurs away from the pure symmetric axis in the wavenumber space. Since their analysis was based on the first-order truncation of an expansion in the zonal wavenumber (associated with a small angle of the bands with respect to the basic shear), Busse & Chen could not quantify the increase of the critical Richardson number as a function of the Prandtl number and, in particular, they could not obtain a result for unity Prandtl number ($Pr = 1$).

Weakly unstable viscous modes were obtained in three-dimensional space by Miller & Antar (1986) for two types of basic flow: Eady baroclinic flow and the rotating Hadley cell of Antar & Fowlis (1983). Their results showed that in the presence of weak diffusivity (Ekman number $Ek \leqslant 0.001$), the pure symmetric mode no longer has the highest growth rate even if $Pr = 1$. Instead, the most unstable mode is horizontally tilted through a small angle to the warm side relative to the basic shear. Horizontally tilted structures with respect to the basic shear were also obtained by Jones & Thorpe (1992) in their numerical simulations of three-dimensional perturbations initialized by small-amplitude symmetric modes, although their nonlinear solution did not reach a steady state and decayed at later time (probably due to the free-slip boundary conditions used in their hydrostatic model).

To the author's knowledge, among the previous publications only Miller & Antar (1986) computed the viscous growth rates for the tilted unstable modes in the Eady basic state. In their study, however, the viscous growth rates were examined only for weak diffusivity ($Ek \leqslant 0.001$) and weak instability (with Ri slightly below the critical value for the symmetric instability). It is not clear how the growth rates will change when the instability and/or diffusivity become strong. The transitional Richardson number, Ri^*, computed in their figure 2 implies that their computed viscous growth rates (with $Ek = 0.001$) preserve the aforementioned features qualitatively for the

inviscid growth rates. This means that (i) the viscous growth rates have two local maxima when the Richardson number is in the vicinity of Ri^*, and (ii) the global maximum point jumps from one local maximum point to the other as the Richardson number changes through Ri^*. These features, however, were not examined in detail. It is also not clear whether and how these features will diminish when the diffusivity becomes strong ($Ek \geqslant 0.005$). Furthermore, the viscous growth rates were presented in Miller & Antar (1986) only as one-dimensional functions of the tilt angle. No growth rate pattern was presented in the two-dimensional space of the horizontal wavelength and tilt angle. The growth rate pattern may provide useful background information for studies of general types of instability, such as the growth of non-modal structures and singular vector perturbations (Farrell & Ioannou 1996; Buizza & Palmer 1995). It will be interesting to see whether and how the growth rate pattern converges to the inviscid one as the Ekman number approaches zero. The above problems will be examined in this paper by using a linearized Boussinesq system of equations with a parameterized (constant) coefficient of turbulent diffusivity. In particular, the spectral model of Gu, Xu & Wu (1998) will be modified to allow not only symmetric but also tilted modes so that it can be used to study the instabilities of baroclinically sheared flows in three-dimensional space.

According to Gu *et al.* (1998), in the presence of diffusivity the most unstable symmetric modes can develop nonlinearly into steady-state circulation bands (provided the horizontal orientation of the bands is constrained in the direction of the symmetric axis along the basic shear), but these nonlinear bands are unstable with respect to four types of normal-mode perturbations in three-dimensional space. The type I mode is characterized by horizontally tilted modes, similar to the tilted primary mode obtained by Miller & Antar (1986). This mode may be viewed as a gradual emergence of the tilted primary mode in three-dimensional space. The remaining three modes are highly three-dimensional and emerge successively as the basic-state Richardson number decreases significantly below the critical value. Since these modes are horizontally more orthogonal than parallel to their parent nonlinear bands (along the basic shear), they do not resemble the tilted primary mode. Thus, if the parent circulation is tilted (developed from the tilted primary mode instead of the symmetric mode), then the type I mode is very likely to disappear but the remaining three modes may still exist. This speculation has not been verified but is more relevant to the real-flow instability in three-dimensional space because the most preferred nonlinear circulation is likely to tilt away from the symmetric axis in the presence of diffusivity. To verify the above speculation and address the related issues, it is necessary to study the primary instabilities of baroclinically sheared flows with respect to tilted modes in three-dimensional space as a first step, and then solve for tilted nonlinear circulations and examine their stability (or secondary instability) with respect to three-dimensional perturbations. This first step has also motivated the current study.

Miller & Antar (1986) and Gu *et al.* (1998) considered only the fully non-slip boundary condition in their studies. Emanuel (1979, 1985) used both the free-slip and non-slip boundary conditions in studies of viscous symmetric instability. He found that the critical condition for the onset of viscous symmetric instability is moderately sensitive to the boundary conditions (see figure 2 of Emanuel 1985). As an extension of viscous symmetric instability, the nearly symmetric instability (associated with the tilted modes) is expected to be also moderately sensitive to the boundary conditions (as long as the Ekman number is not too small). Thus, both types of boundary conditions will be considered in this paper to verify this speculation.

The effect of turbulent eddy diffusivity can be strong in the atmospheric boundary layer and in regions of inertial–symmetric instability as observed on the anticyclonic side of a jet streak (Kennedy & Shapiro 1980; Pepler, Vaughan & Hooper 1998) or within frontal rainbands (Chapman & Browning 2001). Estimated coefficients of eddy diffusivity can vary over a wide range, by an order of magnitude from $O(10)$ to $O(10^2)\,\mathrm{m^2\,s^{-1}}$ in the boundary layer and their orders of magnitudes may also become larger than $O(10^2)\,\mathrm{m^2\,s^{-1}}$ in regions of symmetric instability (Xu 1988). Thus, the range of Ekman number (see (2.9) in § 2) considered in this paper will be sufficiently wide (from 0.0001 to 0.02).

The paper is organized as follows. The model equations and basic-state control parameters are described in the following section, where the system of equations is scaled into a proper non-dimensional form with a reduced number of external-control parameters. The spectral model and method of solution are presented in § 3. Growth rates of the unstable modes are computed and examined in the horizontal wavenumber space for wide ranges of external parameters, in § 4 with the free-slip boundary conditions and in § 5 with the non-slip boundary conditions. Nearly inviscid growth rates are computed in § 6 and compared with results of previous studies. Summary remarks follow in § 7.

2. Model equations and control parameters

2.1. *Basic state and perturbation equations*

The basic state contains a baroclinic flow with a constant vertical shear between two rigid boundaries, say at $z = 0$ and H, and the associated potential temperature field contains a constant gradient in the horizontal as well as in the vertical. This basic state is the same as that in the classic Eady baroclinic model (Eady 1949). Three-dimensional perturbations superimposed on the basic state can be expressed by linear combinations of two-dimensional normal modes. These include both unstable and stable (neutral or decaying) modes, although only unstable modes will be examined in this paper.

The y-coordinate is chosen to be along the banded structure of the normal mode concerned, at an acute angle to the direction of the basic-flow shear. In this coordinate system, the basic-state flow is expressed by

$$\boldsymbol{V} \equiv (U, V) = |\boldsymbol{V}_z|(z - 0.5H)(\sin\alpha, \cos\alpha), \tag{2.1}$$

where $|\boldsymbol{V}_z|$ is the absolute value of the basic shear, H is the depth of the domain, α is the tilt angle (within $\pm 90^\circ$) of the mode (measured negative clockwise from the basic-shear direction to the y-direction, that is to the warm side of the basic shear). The modes concerned satisfy the following linearized Boussinesq system of equations:

$$(\partial_t + U\partial_x)u - fv + w\partial_z U + \partial_x p/\rho_0 = \mu\Delta u, \tag{2.2a}$$

$$(\partial_t + U\partial_x)v + fu + w\partial_z V = \mu\Delta v, \tag{2.2b}$$

$$(\partial_t + U\partial_x)w - b + \partial_z p/\rho_0 = \mu\Delta w, \tag{2.2c}$$

$$(\partial_t + U\partial_x)b + uS_1^2 + vS_2^2 + wN^2 = \kappa\Delta b, \tag{2.2d}$$

$$\partial_x u + \partial_z w = 0, \tag{2.2e}$$

with the free-slip boundary conditions:

$$w = \partial_z u = \partial_z v = \partial_z b = 0 \quad \text{at} \quad z = 0, H, \tag{2.3a}$$

or the non-slip boundary conditions:

$$w = u = v = b = 0 \quad \text{at} \quad z = 0, H, \tag{2.3b}$$

where $\Delta \equiv \partial_x^2 + \partial_z^2$ is the Laplacian operator, (u, v, w) are the three components of the perturbation velocity, p is the perturbation pressure, $b \equiv g\theta/\Theta_0$ is the perturbation buoyancy, θ is the potential temperature, g is the gravitational acceleration, Θ_0 is a constant reference potential temperature,

$$\left(S_1^2, S_2^2, N^2\right) \equiv (g/\Theta_0)(\partial_x, \partial_y, \partial_z)\Theta \tag{2.4}$$

are the three components of the constant gradient of the base-state buoyancy (defined by $g\Theta/\Theta_0$) and Θ is the base-state potential temperature. Also, μ is the coefficient of eddy diffusivity for momentum transport, and κ is the coefficient of eddy diffusivity for heat transport. These two coefficients are assumed to be constant (in the range from 1 to 200 $\mathrm{m^2\,s^{-1}}$) in this paper. The horizontal components of the gradient in (2.4) satisfy the following thermal wind relationship:

$$S_1^2 = f\partial_z V = f|\boldsymbol{V}_z|\cos\alpha, \tag{2.5a}$$

$$S_2^2 = -f\partial_z U = -f|\boldsymbol{V}_z|\sin\alpha, \tag{2.5b}$$

where f is the Coriolis parameter (assumed to be constant).

2.2. *Basic-state parameters and scaling*

The solutions of the above system (2.2)–(2.3) are controlled by the following six independent external parameters:

$$(f, N^2, |\boldsymbol{V}_z|, \mu, \kappa, H). \tag{2.6}$$

The tilt angle, α, is an internal parameter for each normal mode concerned. Exact and approximate similarities exist among the dimensional modes. These similarities can be revealed by scaling the system (2.2)–(2.3) into a proper non-dimensional form with a reduced number of external parameters.

In this paper, $|\boldsymbol{V}_z|H$ is used for the horizontal velocity scale, Hf for the vertical velocity scale, $1/f$ for the time scale, H for the height scale, $L \equiv |\boldsymbol{V}_z|H/f$ for the horizontal length scale which is the Rossby radius of deformation associated with the basic shear or, equivalently, the radius of inertial oscillation associated with the horizontal velocity scale, HN^2 for the buoyancy scale, and $\rho_0 H^2 N^2$ for the pressure scale. The system (2.2)–(2.3) can be then scaled into the following non-dimensional form:

$$\mathrm{D}_t u - v + w\sin\alpha + Ri\,\partial_x p = Ek\,\mathrm{D}u, \tag{2.7a}$$

$$\mathrm{D}_t v + u + w\cos\alpha = Ek\,\mathrm{D}v, \tag{2.7b}$$

$$r^2\mathrm{D}_t w - b + \partial_z p = r^2 Ek\,\mathrm{D}w, \tag{2.7c}$$

$$\mathrm{D}_t b + (u\cos\alpha - v\sin\alpha)/Ri + w = Ek\,\mathrm{D}b/Pr, \tag{2.7d}$$

$$\partial_x u + \partial_z w = 0, \tag{2.7e}$$

with

$$w = \partial_z u = \partial_z v = \partial_z b = 0 \quad \text{at} \quad z = 0, 1, \tag{2.8a}$$

or

$$w = u = v = b = 0 \quad \text{at} \quad z = 0, 1, \tag{2.8b}$$

where $\mathrm{D}_t \equiv \partial_t + (z-0.5)\sin\alpha\partial_x$, $\mathrm{D} \equiv a^2\partial_x^2 + \partial_z^2$, $a \equiv H/L = f/|\boldsymbol{V}_z| = r\sqrt{Ri}$ is the aspect ratio, and

$$Ri \equiv N^2/|\boldsymbol{V}_z|^2 \quad \text{the Richardson number,} \tag{2.9a}$$

$$Ek \equiv \mu/(fH^2) \quad \text{the Ekman number,} \tag{2.9b}$$

$$Pr \equiv \mu/\kappa \quad \text{the Prandtl number,} \tag{2.9c}$$

$$r \equiv f/N \quad \text{the ratio between inertial and buoyancy frequencies.} \tag{2.9d}$$

The independent variables and perturbation variables in (2.7)–(2.8) are all non-dimensional but expressed by the same symbols as the dimensional ones in (2.2)–(2.3). This should not cause confusion since the solutions will be obtained and examined in their non-dimensional forms in the remainder of this paper.

The non-dimensional solutions of (2.7)–(2.8) are controlled by the four external parameters in (2.9). The reduction of the number of independent external-control parameters, from six in (2.6) to four in (2.9), indicates that exact similarities exist among the dimensional solutions along two-dimensional manifolds defined by constant values of the four non-dimensional combinations in (2.9) in the six-dimensional space of the dimensional parameters in (2.6). For the basic state considered in this paper, we have $r^2 = f^2/N^2 \leqslant 0.1$ and $Ri \geqslant 0.25$, so the aspect ratio is small ($a = r\sqrt{Ri} < 0.2$) and the diffusive operator can be approximated by $Ek\,\mathrm{D} \approx Ek\,\partial_z^2$. The smallness of r^2 also suggests $b \approx \partial_z p$ in (2.7c), so the solutions should be nearly hydrostatic and largely independent of r^2 (as verified by the solutions obtained later). Thus, in addition to the above exact similarities, an approximate similarity exists and the non-dimensional solutions are controlled mainly by three external parameters: *Ri*, *Ek* and *Pr*.

3. Spectral representation and method of solution

By introducing the streamfunction, ψ, defined by $u = \partial_z\psi$ and $w = -\partial_x\psi$, the five-equation system (2.7)–(2.8) reduces to the following system:

$$\mathrm{D}_t\mathrm{D}\psi + Ri\,\partial_x b - \partial_z v = Ek\,\mathrm{D}^2\psi, \tag{3.1a}$$

$$\mathrm{D}_t v + \partial_z\psi - \partial_x\psi\cos\alpha = Ek\,\mathrm{D}v, \tag{3.1b}$$

$$\mathrm{D}_t b + (\partial_z\psi\cos\alpha - v\sin\alpha)/Ri - \partial_x\psi = Ek\,\mathrm{D}b/Pr, \tag{3.1d}$$

with

$$\psi = \partial_z^2\psi = \partial_z v = \partial_z b = 0 \quad \text{at} \quad z = 0, 1, \tag{3.2a}$$

or

$$\psi = \partial_z\psi = v = b = 0 \quad \text{at} \quad z = 0, 1, \tag{3.2b}$$

where (3.1a) is the along-band vorticity equation derived from $\partial_z(2.7a) - Ri\,\partial_x(2.7c)$ by eliminating the pressure terms, and the mass continuity equation (2.7e) is automatically satisfied. Using (3.1)–(3.2), the normal-mode solutions can be obtained conveniently in three component fields, (ψ, v, b), instead of five component fields, (u, v, w, p, b), as in the original system (2.7)–(2.8).

Since the y-coordinate is chosen to be along the banded structure of each normal mode concerned, the structure of the mode is uniform in the y-direction and periodic in the x-direction. Thus, the solution can be expressed by the following spectral

expansions:

$$\psi = \sum_{n=1}^{\infty} \psi_n g_n(z) \exp[\mathrm{i}kx + (\sigma - \mathrm{i}\omega)t)], \tag{3.3a}$$

$$v = \sum_{n=0}^{\infty} v_n q_n(z) \exp[\mathrm{i}kx + (\sigma - \mathrm{i}\omega)t)], \tag{3.3b}$$

$$b = \sum_{n=0}^{\infty} b_n q_n(z) \exp[\mathrm{i}kx + (\sigma - \mathrm{i}\omega)t)], \tag{3.3c}$$

where $k\,(\geqslant 0)$ is the horizontal wavenumber, σ is the growth rate, and ω is the frequency observed in the coordinate system that moves with the middle-level basic flow (see (2.1)). Since α, σ and ω can be either positive or negative, here k is assumed to be non-negative without loss of generality.

For the free-slip case, the two sets of basis functions, $g_n(z)\,(n=1, 2, \ldots)$ and $q_n(z)$ $(n=0, 1, 2, \ldots)$, are given by the eigenfunctions of $(\partial_z^4 - \lambda_n^4)g_n(z)=0$ and $(\partial_z^2 + \gamma_n^2)q_n(z)=0$ with the free-slip boundary conditions of $\partial_z^2 g_n(z) = g_n(z)=0$ and $\partial_z q_n(z)=0$ at $z=0, 1$. It is easy to see that the eigenvalues are given by $\lambda_n = \gamma_n = n\pi$, and the eigenfunctions have the following simple forms:

$$g_n(z) = \sin(n\pi z), \tag{3.4a}$$

$$q_n(z) = \cos(n\pi z). \tag{3.4b}$$

For the non-slip case, the two sets of basis functions in (3.4) should be replaced by those in (3.4) of Gu *et al.* (1998). These non-slip basis functions are still denoted by $g_n(z)$ and $q_n(z)$ $(n = 1, 2, \ldots)$ but given by the eigenfunctions of $(\partial_z^4 - \lambda_n^4)g_n(z) = 0$ and $(\partial_z^2 + \gamma_n^2)q_n(z) = 0$ with the non-slip boundary conditions of $\partial_z g_n(z) = g_n(z) = 0$ and $q_n(z) = 0$ at $z = 0, 1$. In this case, $q_n(z) = \sin(n\pi z/H)$ as in (3.4*b*) of Gu *et al.* (1998), so $q_0(z) = 0$, that is the zeroth eigenfunction is trivial and should be removed from the summations in (3.3*b*) and (3.3*c*). The above basis functions for either the free-slip or non-slip case are complete in the sense that they can construct all the vertical modes for the solutions of (3.1)–(3.2). The normal-mode solutions expressed by (3.3) are controlled by two internal parameters: k and α. Note that (k, α) is the polar-coordinate representation of the horizontal vector wavenumber, $(k\cos\alpha, k\sin\alpha)$, with respect to the direction of the basic shear. The normal modes expressed by (3.3) for the entire spectral space of $(k\cos\alpha, k\sin\alpha)$ are complete in the sense they can construct any three-dimensional solutions of the linearized Boussinesq system of equations.

Substituting truncated forms of (3.3) (n up to M) into (3.1) and then projecting the three resulting equations onto the basis functions $g_n(z)$, $q_n(z)$ and $q_n(z)$, respectively, we obtain a set of linear algebraic equations for the complex eigenvalue problem in which $(\sigma - \mathrm{i}\omega)$ is the complex eigenvalue and the eigenvector is composed of $\{\psi_n \,|\, n = 1, 2, \ldots M\}$ and $\{(v_n, b_n) \,|\, n = 0, 1, 2, \ldots M\}$ for the free-slip case or $\{(\psi_n, v_n, b_n) \,|\, n = 1, 2, \ldots M\}$ for the non-slip case. A solution obtained from this set of equations can be substituted into (3.3) to yield a truncated vertical mode (for fixed k and α). Since the dimension of this set of algebraic equations is $3M+2$ for the free-slip case or $3M$ for the non-slip case, the number of truncated vertical modes that can be obtained is $3M+2$ or $3M$. Among these vertical modes, only the most unstable one (that has the largest growth rate σ for fixed k and α) will be considered. The solutions are found to converge rapidly as M increases to 12, and become sufficiently accurate when $M = 20$

as long as the Ekman number is not too small ($Ek \geqslant 5 \times 10^{-3}$). Thus, $M = 20$ is used for the solutions presented in the next two sections. For the nearly inviscid modes obtained (with $Ek = 10^{-4}$) in § 6.2, $M = 40$ is used to ensure the accuracy of the solutions.

4. Growth rate pattern and its dependence on external parameters for free-slip case

4.1. *Growth rate pattern*

For mid-latitude mesoscale frontal rainbands, the following are typical values for the dimensional external parameters: $f = 10^{-4}\,\mathrm{s}^{-1}$, $N^2 = 0.5 \times 10^{-6}\,\mathrm{s}^{-2}$, $|\boldsymbol{V}_z|^2 = 10^{-6}\,\mathrm{s}^{-2}$, $H = 10^4\,\mathrm{m}$, and $\mu = \kappa = 100\,\mathrm{m}^2\,\mathrm{s}^{-1}$. This yields $Ri = 0.5$, $Ek = 0.01$, $Pr = 1$ and $r^2 = 0.02$ for the non-dimensional parameters in (2.9). We may also choose typical values of $N^2 = 0.5 \times 10^{-5}\,\mathrm{s}^{-2}$ and $|\boldsymbol{V}_z|^2 = 10^{-5}\,\mathrm{s}^{-2}$ to represent a basic state with relatively strong vertical stratification and vertical shear. This yields the same non-dimensional parameter values except that r^2 decreases from 0.02 to 0.002. Since the growth rate pattern changes only slightly when r^2 decreases from 0.02 to 0.002 (see § 4.2), we will simply choose 0.02 as a reference value for r^2. With this set of external parameter values, unstable modes are sought over a wide range in the internal parameter space (l, α) where $l = 2\pi/k$ is the horizontal wavelength and α is defined in (2.1).

The computed growth rates are plotted as a function of (l, α) for $\sigma \geqslant 0$ in figure 1(*a*). Note that $\sigma(l, \alpha)$ is periodic in the α-direction and the plotted pattern is repeated as α goes beyond $\pm 90^\circ$. Here, the symmetric axis is along $\alpha = 0$ while the baroclinic axis is along $\alpha = -90^\circ$ or 90° (due to the periodicity). As shown in figure 1(*a*), unstable modes exist over a broad area extended to the long-wavelength side except for a narrow strip in the vicinity (mainly on the positive side) of $\alpha = 0$. The growth rates are below zero along the symmetric axis, so the basic state is stable with respect to symmetric perturbations. The main growth rate pattern has two branches on the two sides of the symmetric axis. These two branches are connected into a single pattern (banana-shaped for $\sigma \geqslant 0.1$) in the periodic domain, say over the range of $0^\circ \leqslant \alpha \leqslant 180^\circ$. The maximum growth rate is 0.300 at the point $(l, \alpha) = (1.06, -11^\circ)$ in the main growth rate pattern. There is neither a secondary maximum in the main growth rate pattern nor a local maximum in the side lobe attached to the concave lower edge of the lower branch of the main growth rate pattern.

Except for the modes within the side lobe, all the unstable modes have zero frequency ($\omega = 0$), so they do not propagate with respect to the middle-level basic flow (see (2.1) and (3.3)). Within the side lobe, the growth rate decreases gradually to zero but the frequency increases nearly linearly from $\omega = 0$ to about $\omega = 3.0$ (not shown) as the parameter point (l, α) moves downward and leftward away from the concave lower edge of the main growth rate pattern to the lower-left boundary of the side lobe. In association with each non-zero ω, there is a pair of conjugate-complex eigenvalues: $\sigma \pm \mathrm{i}|\omega|$. In association with this pair of eigenvalues, the two vertical modes have the same growth rate and propagate with the same phase speed of $|\omega|/k$ but in opposite directions with respect to the middle-level basic flow.

4.2. *Exact and approximate similarities*

With the above external parameter values, the scale height is chosen to be $H = 10^4\,\mathrm{m}$, which is the typical depth of the troposphere. Frontal rainbands, however, are often shallower or much shallower than the troposphere (Browning, Chapman & Dixon 2001). In view of this, we choose $H = h \times 10^4\,\mathrm{m}$, where h is a fraction factor ranging

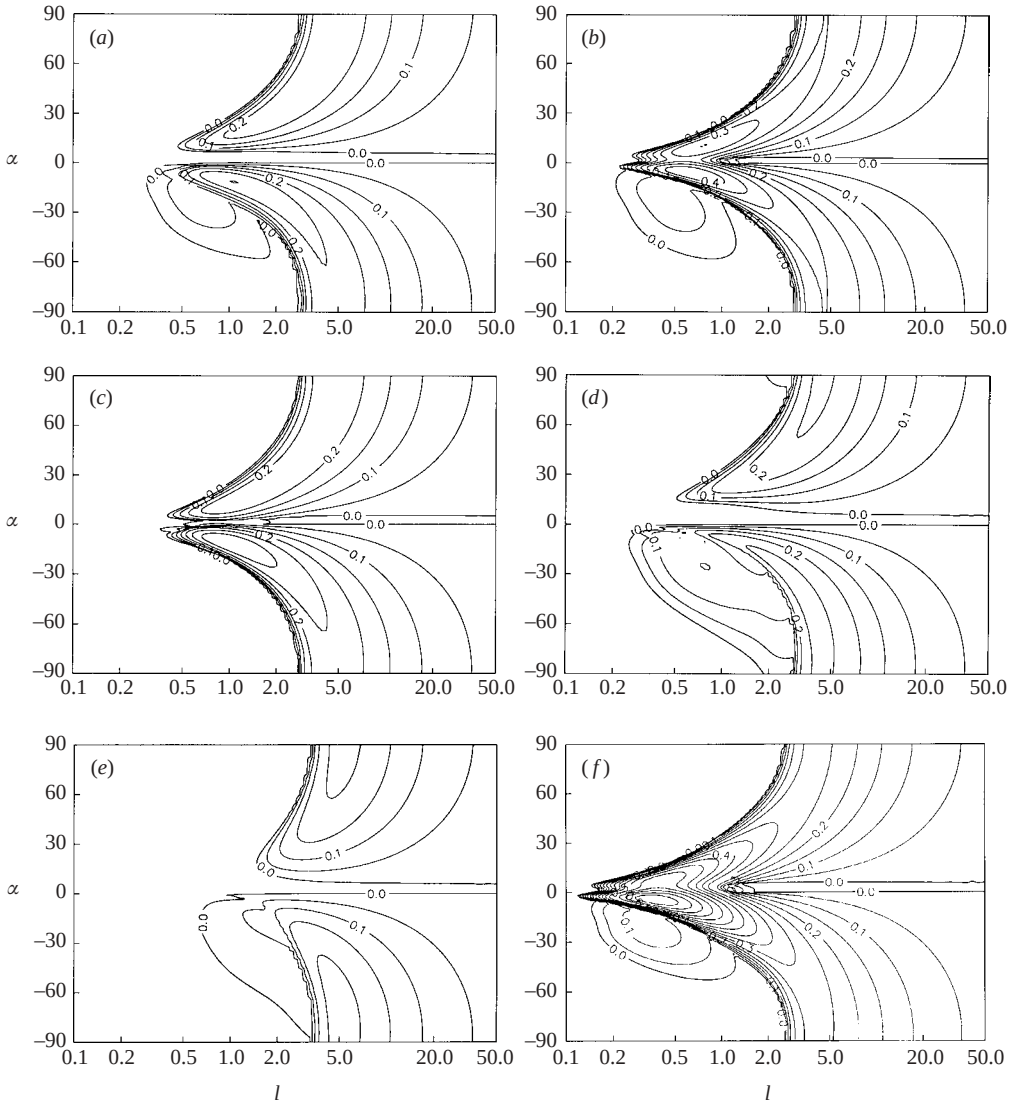

FIGURE 1. (*a*) Growth rate obtained with the free-slip boundary conditions in (3.2) and plotted as a function of (l, α) for $\sigma \geqslant 0$, where $l = 2\pi/k$ (plotted in logscale) is the wavelength and α is the tilt angle (within $\pm 90^\circ$) of the mode (measured negative clockwise from the basic-shear direction to the y-direction, that is to the warm side of basic shear). The external parameter values are $Ri = 0.5$, $Ek = 0.01$, $Pr = 1.0$ and $r^2 = 0.02$. The global maximum growth rate is $\sigma = 0.300$ at $(l, \alpha) = (1.06, -11^\circ)$. (*b*) As in (*a*) but for $Ek = 0.005$. The global maximum growth rate is $\sigma = 0.445$ at $(l, \alpha) = (0.65, -6^\circ)$. (*c*) As in (*a*) but for $Pr = 2.0$. (*d*) As in (*a*) but for $Pr = 0.5$. (*e*) As in (*a*) but for $Ri = 1.0$. (*f*) As in (*a*) but for $Ri = 0.25$.

from 0.2 to 1. Also, the eddy diffusivity may be relatively weak for relatively shallow rainbands, so we choose $\mu = h^2 \times 100\,\mathrm{m^2\,s^{-1}}$ to obtain the same non-dimensional parameter values as in figure 1(*a*). For example, the result in figure 1(*a*) can be applied to a class of external parameter values generated by different values of h. As explained in § 2, the exact similarities among the dimensional solutions allow us

to apply the non-dimensional results obtained in this paper to broad ranges of the external parameters in dimensional space.

It was also mentioned in § 2 that an additional approximate similarity exists among the dimensional modes since the non-dimensional solutions are largely independent of r^2 (for $r^2 \leqslant 0.1$). This is verified by the growth rates computed for the same $Ri = 0.5$ and $Ek = 0.01$ as in figure 1(a) but with different values of r^2. For example, when r^2 is doubled from 0.02 to 0.04, the maximum growth rate decreases very slightly from 0.300 to 0.294 and the maximum point also shifts slightly from (1.06, $-11°$) to (1.129, $-12°$). There is almost no visible change in the growth rate pattern (not shown). When r^2 is halved from 0.02 to 0.01, the maximum growth rate increases slightly from 0.300 to 0.304 and the maximum point shifts slightly from (1.06, $-11°$) to (0.997, $-11°$). Again, there is almost no visible change in the growth rate pattern (not shown). As r^2 further decreases, say to 0.001, the maximum growth rate increases slightly to 0.307, the maximum point has no detectable shift and is still at (0.997, $-11°$), and the growth rate pattern becomes nearly independent of r^2. Thus, there is indeed an approximate similarity between different values of r^2. We will only examine the dependence of the growth rates on (Ek, Pr, Ri) in the remainder of this section.

4.3. *Dependence on Ekman number*

When the Ekman number is doubled to 0.02 from the value in figure 1(a), the main growth rate pattern shrinks towards the long-wavelength side and the two branch 'noses' retreat from $l \approx 0.5$ to $l \approx 1.0$ and become slightly further apart from each other and away from the symmetric axis (not shown). The maximum growth rate decreases from 0.300 to 0.255, and the maximum point shifts from (1.06, $-11°$) to (2.69, $-32°$). When the Ekman number is halved to 0.005, the growth rate pattern expands and becomes connected across the symmetric axis (see figure 1(b)). The maximum growth rate increases to 0.445 and the maximum point shifts to (0.65, $-6°$). Also, two local maxima emerge in the growth rate pattern. One is the secondary maximum of $\sigma = 0.350$ at $(l, \alpha) = (0.78, 11°)$ on the positive-α side of the symmetric axis in the main growth rate pattern, and the other is the local maximum of $\sigma = 0.06$ with $\omega = 3.02$ at $(l, \alpha) = (0.418, -32°)$ within the side lobe. As in figure 1(a), the unstable modes in the main growth rate pattern are all non-propagating, while the unstable modes within the side lobe are all propagating. Clearly, the smaller the Ekman number becomes, the shorter the wavelength and the closer to the symmetric axis the horizontal orientation of the most unstable mode. These general features are also seen from the growth rate patterns obtained with $Ek = 0.002$, 0.001 and 0.0001 (not shown).

4.4. *Dependence on Prandtl number*

When the Prandtl number is doubled to 2.0 from the value in figure 1(a), the maximum growth rate increases from 0.300 to 0.345 and the maximum point shifts slightly from (1.06, $-11°$) to $(l, \alpha) = (1.00, -11°)$. The lower branch shifts upward slightly across the symmetric axis and the upper branch shifts downward slightly (figure 1(c)). The gap between the two branches is thus nearly closed and is filled by a narrow side lobe over the range $0.5 \leqslant l \leqslant 2.0$ along the symmetric axis. The original side lobe (attached to the concave lower edge of the main growth rate pattern in figure 1a) disappears. In comparison with figure 1(a), the overall change of the main growth rate pattern in figure 1(c) is roughly similar to that in figure 1(b).

When the Prandtl number is halved to 0.5, the maximum growth rate decreases to 0.263 and the maximum point shifts significantly from (1.06, $-11°$) to (3.05, $-37°$). In this case, as shown in figure 1(d), the gap between the two branches of the main

growth rate pattern is widened (to about twice that in figure 1*a*) over the range $0.5 \leqslant l \leqslant 2.0$, and the side lobe becomes more than twice as large as that in figure 1. Within the side lobe, the growth rate pattern has a local maximum of $\sigma = 0.063$ with $\omega = 3.06$ at $(l, \alpha) = (0.418, -35^\circ)$. As explained above, propagating unstable modes exist only within the side lobe. Note also that the lower branch of the main growth rate pattern shrinks towards the long-wavelength side and the lower branch 'nose' retreats from $l \approx 0.5$ to $l \approx 0.8$ below the symmetric axis. The overall change of the main growth rate pattern is somewhat similar to that obtained when the Ekman number is doubled from $Ek = 0.01$ to 0.02 (as described in § 4.3).

Note that a doubling of Pr (with Ek fixed) means a halving of κ, while a halving of Ek (with Pr fixed) means a halving of both μ and κ. When Ek is fixed, the change of the growth rates with Pr shows partially the effect of κ versus μ and partially the effect of the overall diffusivity (that is, the combined effect of μ and κ on the growth rate). This may partly explain why the overall change in the main growth rate pattern caused by doubling (or halving) Pr from 1.0 to 2.0 (or 0.5) is similar to that caused by halving (or doubling) Ek from 0.01 to 0.005 (or 0.02). Thus, $Ek/\sqrt{Pr} = (\mu\kappa)^{1/2}/(fH^2)$ can be introduced as a modified Ekman number to measure the overall diffusivity. When $Ek/\sqrt{Pr}$ is fixed instead of Ek, the change in the growth rates with Pr is constrained by the fixed overall diffusivity, so the dependence of the growth rate pattern on Pr should be reduced in certain respects and this is observed from the computed growth rate patterns (not shown).

4.5. *Dependence on Richardson number*

When the Richardson number is doubled to 1.0 from the value in figure 1(*a*), the growth rate pattern shifts to the long-wavelength side (see figure 1(*e*)). The maximum growth rate decreases from 0.300 to 0.216 and the maximum point shifts dramatically from (1.06, -11°) to (5.02, -74°). When the Richardson number is halved to 0.25, the growth rate pattern expands towards the short-wavelength side and becomes connected across the symmetric axis (see figure 1*f*). The lower and upper branches of the main growth rate pattern become very close to the symmetric axis and extend leftward from $l \approx 0.5$ to $l \approx 0.12$ and 0.15, respectively. The side lobe is also shifted with the lower branch to the short-wavelength side. The size and shape of the side lobe remain roughly the same as in figure 1(*a*), but a local maximum of $\sigma = 0.116$ emerges at $(l, \alpha) = (0.31, -25^\circ)$ with $\omega = 3.11$ within the side lobe. The (global) maximum growth rate increases from 0.300 to 0.79 and the maximum point shifts from (1.06, -11°) to (0.37, -4°). Clearly, the smaller the Richardson number becomes, the shorter the wavelength and the closer to the symmetric axis the horizontal orientation of the most unstable mode.

5. Growth rate pattern and its dependence on external parameters for the non-slip case

As originally intended by Eady (1949), the upper rigid boundary may represent the effect of the tropopause on the tropospheric flows. However, in the presence of diffusivity, the Eady basic state cannot be sustained without heat and momentum fluxes through the upper and lower boundaries. In other words, the basic-state baroclinic shear needs to be supported by the relative motions of the upper and lower boundaries while the basic-state potential temperature gradient needs to be supported by the thermal conductivity at the upper and lower boundaries. This implies that the boundary conditions should be fully non-slip (that is, thermally conductive and

kinematically non-slip) for the basic state as well as for the perturbations (see § 2 of Xu 1987). With the free-slip boundary conditions used in (3.2*a*), the basic state itself is not exactly a steady-state solution of the current model, unless it is maintained by some kind of external forcing (such as a horizontal gradient of radiative heating) not explicitly described in the current model. The free-slip boundary conditions in (3.2*a*) may be more realistic than the non-slip boundary conditions in representing the effect of the tropopause, but the non-slip boundary conditions should be more realistic in representing the Earth's rigid surface. If the non-slip boundary conditions are used only at the lower boundary, then the basic state still needs to be maintained by some kind of external forcing. In this case, all the unstable modes will propagate with respect to the middle-level basic flow and thus the growth rates cannot be compared with those in the previous results of Miller & Antar (1986). Because of this, as shown in (3.2*b*), the non-slip boundary conditions are used at both the lower and upper boundaries. These non-slip boundary conditions are the same as in Emanuel (1979, 1985), Miller & Antar (1986) and Gu *et al.* (1998). Thus, the sensitivity of the growth rates to the boundary conditions can be examined in comparison with results of Emanuel (see § 5.5), the growth rates obtained with (3.2*b*) can be precisely compared to the previous results of Miller & Antar (see § 6.1), and the unstable modes obtained with (3.2*b*) can be used for a further study of nonlinear perturbations to verify the speculation in the introduction based on the results of Gu *et al.* (1998).

5.1. *Growth rate pattern*

With the non-slip boundary conditions in (3.2*b*), growth rates are computed for the same external parameter values as in figure 1(*a*) and the pattern is plotted (for $\sigma \geqslant 0$) in figure 2(*a*). As shown, unstable modes exist over a banana-shaped area with l ranging from 0.37 to 10.0 and α ranging from -153° to 1° (or, equivalently, from 27° to 181°). The maximum growth rate is 0.246 at $(l, \alpha) = (0.93, -12^\circ)$. Along the symmetric axis, the growth rate has a conditional maximum of $\sigma = 0.066$ at $l = 0.81$. This conditional maximum corresponds to the most unstable symmetric mode and is much smaller than the global maximum (0.246). The unstable modes on the symmetric axis are associated with the classic symmetric instability and will be called symmetric modes; while the unstable modes on the baroclinic axis ($\alpha = \pm 90^\circ$) are associated with the classic Eady baroclinic instabilities (except for the inclusion of diffusivity) and will be called baroclinic modes in this paper.

The sensitivity of the growth rates to the type of boundary conditions can be examined by comparing figure 2(*a*) with figure 1(*a*). In figure 2(*a*), the growth rate pattern drops below zero on the long-wavelength side, the upper branch retreats further away from the symmetric axis, and the side lobe disappears. The global maximum of the growth rate pattern, however, is still quite close to that in figure 1(*a*). Thus, the growth rates are moderately sensitive to the boundary conditions.

5.2. *Exact and approximate similarities*

The same types of exact and approximate similarities exist for the non-slip case as explained for the free-slip case in § 4.2. The approximate similarity is verified by the growth rate patterns computed with r^2 varying over a wide range of values. For example, when r^2 is doubled from 0.02 to 0.04, the maximum growth rate decreases slightly from 0.246 to 0.240 and the maximum point shifts also slightly from (0.93, -12°) to (0.96, -12°). There is almost no change in the growth rate pattern (not shown). When r^2 is halved from 0.02 to 0.01, the maximum growth rate increases slightly from 0.246 to 0.250 and the maximum point shifts slightly from (0.93, -12°) to (0.90, -11°). As r^2 further decreases, say to 0.001, the maximum growth rate

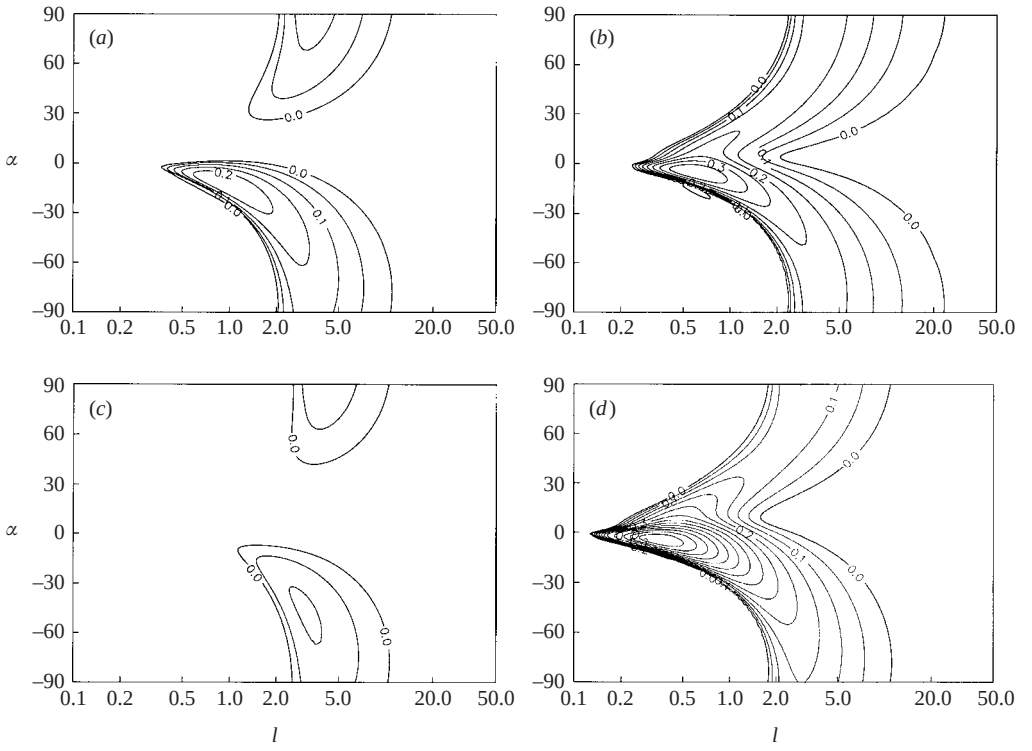

FIGURE 2. Growth rate obtained for the same external parameter values as in figure 1(*a*) but with the non-slip boundary conditions in (3.2*b*). The global maximum is at $(l, \alpha) = (0.93, -12°)$. (*b*) As in (*a*) but for $Ek = 0.005$. (*c*) As in (*a*) but for $Ri = 1.0$. (*d*) As in (*a*) but for $Ri = 0.25$.

increases slightly to 0.253, the maximum point shifts slightly to (0.88, −11°), and the growth rate pattern becomes nearly independent of r^2.

5.3. *Dependence on Ekman number*

When the Ekman number is doubled to 0.02, the growth rate pattern shrinks, the lower branch detaches from the symmetric axis, and the upper branch retreats upward across the baroclinic axis to $\alpha = 93°$ (not shown). The maximum growth rate decreases from 0.246 to 0.135 and the maximum point shifts from (0.93, −12°) to (1.19, −21°). When the Ekman number is halved to 0.005, the growth rate pattern expands and becomes connected in the α-direction (figure 2(*b*)). The maximum growth rate increases to 0.398 and the maximum point shifts to (0.60, −5°). Clearly, the smaller the Ekman number becomes, the shorter the wavelength and the closer to the symmetric axis the horizontal orientation of the most unstable mode. The unstable modes in figure 2(*b*) are mostly non-propagating (with $\omega = 0$), except for those in the small side lobe attached to the lower edge of the main growth rate pattern around $(l, \alpha) = (0.6, -20°)$ in figure 2(*b*). In this small side lobe, ω is very close, but not identical, to zero. By comparing figure 2(*b*) with figure 1(*b*), we can see that the growth rates are moderately sensitive to the boundary conditions.

5.4. *Dependence on Prandtl number*

When the Prandtl number is doubled to 2.0, the maximum growth rate increases slightly to 0.248 and the maximum point shifts slightly to (0.88, −11°), but the growth rate pattern expands and becomes connected across the symmetric axis (not shown).

The change of the overall growth rate pattern is roughly similar to that in figure 2(*b*). When the Prandtl number is halved from 1.0 to 0.5, the maximum growth rate increases from 0.246 to 0.261, the maximum point shifts from (0.93, $-12°$) to (0.94, $-13°$), the upper branch of the growth rate pattern retreats upward from $\alpha = 27°$ to about 50°, and a side lobe emerges underneath the concave lower edge of the main growth rate pattern (not shown). The overall change of the main growth rate pattern caused by doubling (or halving) Pr is similar to that caused by halving (or doubling) Ek. This rough similarity may be partially explained in the same way as for the free-slip case in § 4.4. When $Ek/\sqrt{Pr}$ is fixed instead of Ek, the dependence of the growth rate pattern on Pr is reduced (see the comparisons of the dashed and dotted curves in figure 5 with those in figure 10 of Miller & Antar 1986).

5.5. *Dependence on Richardson number*

When the Richardson number is doubled to 1.0, the growth rate pattern shrinks toward the long-wavelength side and away from the symmetric axis (see figure 2(*c*)). The maximum growth rate decreases from 0.246 to 0.106 and the maximum point shifts from (0.93, $-12°$) to (3.13, $-47°$). When the Richardson number is halved to $Ri = 0.25$, the growth rate pattern expands and becomes connected across the symmetric axis (see figure 2*d*). The maximum growth rate increases to 0.69 and the maximum point shifts to (0.35, $-4°$). Clearly, the smaller the Richardson number becomes, the shorter the wavelength and the closer to the symmetric axis the horizontal orientation of the most unstable mode.

By comparing figure 2(*c*, *d*) with figure 1(*e*, *f*), we can see again that the growth rates are moderately sensitive to the boundary conditions. This and the above comparisons of the growth rates obtained with the two types of boundary conditions are qualitatively consistent with the results obtained by Emanuel (1979, 1985) for the onset of viscous symmetric instability. As an extension of viscous symmetric instability, the nearly symmetric instability (associated with the tilted modes) is also moderately sensitive to the boundary conditions (as long as the Ekman number is in the range $0.005 \leqslant Ek \leqslant 0.02$).

6. Comparisons with previous results for nearly inviscid and inviscid cases

As mentioned in the introduction, when the Richardson number is in the range $1 > Ri > 0.84$, the inviscid growth rate pattern has two local maxima. One is the symmetric local maximum at $(l, \alpha) = (0, 0)$ or $(k\cos\alpha, k\sin\alpha) = (\infty, 0)$ while the other is the baroclinic local maximum on the baroclinic axis defined by $\alpha = \pm 90°$ or $k\cos\alpha = 0$. The global maximum is the symmetric one if $Ri^* > Ri > 0.84$, and the baroclinic one if $1 > Ri > Ri^*$, where $Ri^* = 0.95$ is the transitional Richardson number. As the Richardson number changes through Ri^*, the global maximum point jumps from one local maximum point to the other in the space of the horizontal wavenumber $(k\cos\alpha, k\sin\alpha)$ or in the space of (l, α). These features, however, are not seen from the viscous growth rates obtained with $Ek \geqslant 0.005$ in the previous sections. Thus, the growth rate patterns change not only quantitatively but also qualitatively when Ek increases from zero to 0.005 for both the free-slip and non-slip cases. This addresses only the first of the questions raised in the introduction. The remaining questions concern whether and how the viscous growth rate pattern (obtained for a given set of external parameters) will converge to the inviscid one as the Ekman number decreases towards zero. To address these questions, we will first reduce Ek to 0.001 and compare with results from Miller & Antar (1986) for the non-slip case in

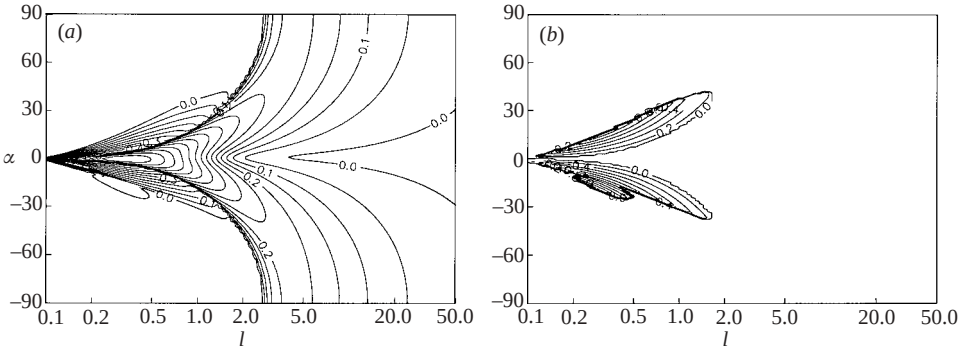

FIGURE 3. Growth rate $\sigma\,(a)$ and frequency $\omega\,(b)$ plotted as functions of (l, α) for $\sigma \geqslant 0$ for the non-slip case. The external parameter values are as in figure 2(a) except that $Ek = 0.001$. The maximum growth rate is 0.736 and the maximum point is at $(l, \alpha) = (0.347, -0.29°)$.

§ 6.1 and, then, further reduce Ek to 0.0001 and compare with the inviscid results of Stone (1970) in § 6.2.

6.1. *Comparisons with nearly inviscid results of Miller & Antar*

The four non-dimensional external parameters used in Miller & Antar (1986) are: Ri, Ek, Pr and Ro, where the first three parameters are the same as ours in (2.9a)–(2.9c) and the last is the shear Rossby number defined by $Ro \equiv |\boldsymbol{V}_z|/f$. Note that $Ro = 1/(r\sqrt{Ri}) = L/H = 1/a$, so Ro is also the inverse of the aspect ratio defined in this paper. As shown in §§ 4 and 5 the non-dimensional modes are nearly independent of r but strongly dependent on Ri. This implies that the non-dimensional modes are dependent on Ro through the relationship $Ro = 1/(r\sqrt{Ri})$. Thus, using r instead of Ro as the last external parameter simplifies the problem studied here. Since the horizontal length scale was chosen to be the same as the height scale in Miller & Antar (1986), $Ro = L/H$ is the ratio between the two horizontal length scales used here and in their study. This ratio needs to be considered when the wavelengths are compared. The time scale used here is the same as theirs, so the non-dimensional growth rates can be compared directly.

In this section, Ek is reduced to 0.001 to match the Ekman number used by Miller & Antar (1986). Recall that $Ek = 0.005$ in figure 1(b). When this value is reduced by a factor 5 to $Ek = 0.001$, the growth rate pattern becomes nearly symmetric with respect to the symmetric axis (figure 3a) and propagating unstable modes (with $\omega \neq 0$) emerge in the two side lobes attached to the lower and upper edges of the main growth rate pattern (figure 3b). The maximum growth rate increases to 0.736 and the maximum point moves to $(0.347, -0.29°)$. The main growth rate pattern becomes very close to the inviscid one.

Miller & Antar (1986) sought the conditional maximum growth rates with l varied but α fixed. The results were plotted as functions of α in their figure 4 for $Pr = 1$, $Ro = 20$, $Ek = 0.001$, $Ri = 0.8$ and 0.92. Note that $r^2 = 1/(Ro^2 Ri)$, so $Ro = 20$ is equivalent to $r^2 = 0.0025/Ri$. This relationship is used to set the parameters in figures 4(a) and 4(b) corresponding to their figures 4(c) and 4(a), respectively. Along the ridge of the growth rate topography in figure 4(a) or figure 4(b) one can see how the conditional maximum growth rate σ and associated wavelength l change as functions of α. The conditional maximum growth rate obtained from figure 4(a) is plotted as the upper solid curve in figure 5. This curve has the same shape as that

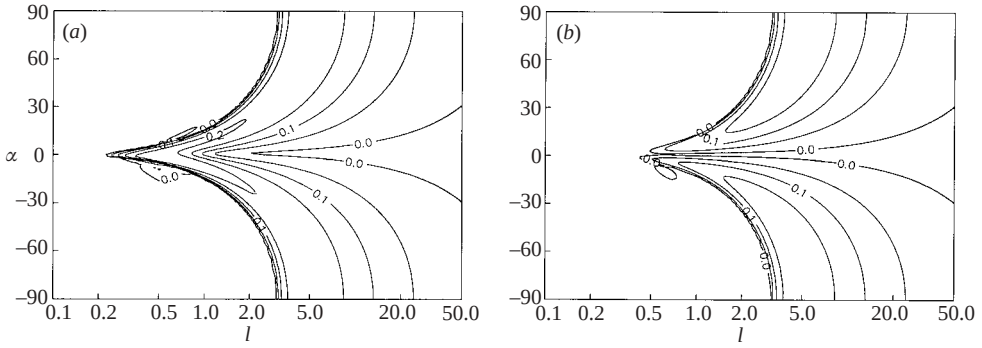

FIGURE 4. As in figure 3(*a*) except that $Ri = 0.8$ and $r^2 = 0.0025/Ri$. (*b*) As in (*a*) except that $Ri = 0.92$.

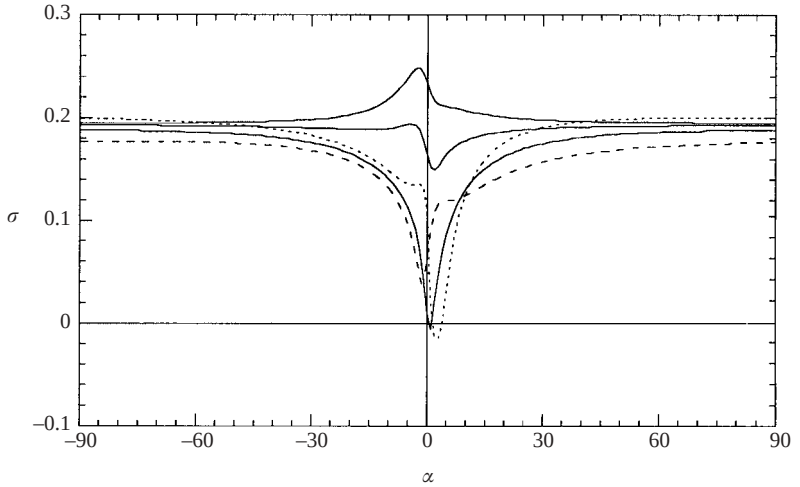

FIGURE 5. Conditional maximum growth rates for the non-slip case, plotted as functions of α for $Ri = 0.8$ and $Pr = 1$ (upper solid curve), $Ri = 0.92$ and $Pr = 1$ (lower solid curve), $Ri = Ri^* = 0.84$ and $Pr = 1$ (middle solid curve), $Ri = 0.92$ and $Pr = 2.0$ (dashed curve), and $Ri = 0.92$ and $Pr = 0.5$ (dotted curve) with $r^2 = 0.0025/Ri$ and fixed $Ek/\sqrt{Pr} = 0.001$.

in figure 4(*c*) of Miller & Antar (1986), but with only 1/4 the amplitude. When the results are further compared with the analytically obtained inviscid growth rates for the symmetric mode ($\sigma = 0.38$ at $\alpha = 0$ and $l = 0.50$) and baroclinic mode ($\sigma = 0.22$ for $l = 4.7$), it appears that the growth rate in their figure 4(*c*) was not correctly scaled and should be reduced by a factor 4.

By comparing figure 4(*a*) and figure 3(*a*), one can see how the growth rate pattern changes as the Richardson number increases from 0.5 to 0.8. (Note that $r^2Ri = 0.01$ in figure 3(*a*) and decreases to 0.0025 in figure 4(*a*), but this causes almost no change in the growth rate pattern). The major changes caused by the increase of the Richardson number are as follows: (i) the two side lobes are diminished; (ii) the main growth rate pattern is shifted to the long-wavelength side while the maximum growth rate is decreased from 0.736 to 0.249 and the maximum point is moved from (0.347, $-0.29°$) to (0.535, $-2.1°$).

Figure 4(*b*) shows how the growth rate pattern changes as the Richardson number increases further from 0.8 to 0.92 with $r^2Ri = 0.0025$ fixed. The major changes compared to figure 4(*a*) are as follows: (i) the upper side lobe has completely disappeared and the lower side lobe is further reduced; (ii) the V-shape ridge has collapsed into a 'canyon' (with $\sigma < 0$) along the symmetric axis. In this case, although the maximum growth rate decreases only slightly from 0.249 to 0.188, the maximum point jumps from (0.535, $-2.1°$) to (5.02, 89°). The conditional maximum growth rate is plotted as the lower solid curve in figure 5. This curve has the same shape as that in figure 4(*a*) of Miller & Antar (1986) (although the amplitudes are different by a factor 4 for the same reason mentioned earlier). Multiplied by the ratio between the two horizontal length scales ($Ro = L/H = 20$), the associated wavelength (not shown) is found to be the same as that in figure 4(*b*) of Miller & Antar (1986).

The jump of the maximum growth rate point in response to the increase of Ri from 0.8 in figure 4(*a*) to 0.92 in figure 4(*b*) implies the existence of a transitional Richardson number (within the range $0.8 < Ri^* < 0.92$). When Ri is in the vicinity of Ri^*, the growth rate pattern has two local maxima. The global maximum jumps from one local maximum to the other as Ri increases through Ri^*. Miller & Antar (1986) plotted Ri^* as a function of Ro for $Pr = 1.0$ and $Ek = 0.001$ in their figure 2, showing that Ri^* is nearly constant ($Ri^* = 0.84$) when $Ro \geqslant 7.5$. Note that the latter condition ($Ro \geqslant 7.5$) is equivalent to $r^2 = (Ro^2Ri^*)^{-1} \leqslant (47.25)^{-1} < 0.02$, so Ri^* is nearly constant for the entire range of r^2 considered in this paper. When $Ri = Ri^*(= 0.84)$, the growth rate pattern (not shown) has two local maxima with the same growth rate of $\sigma = 0.194$. These two local maxima are located near the symmetric and baroclinic axes, respectively. As shown by the conditional maximum growth rate (middle solid curve) in figure 5, one local maximum is at $\alpha = -4°$ and the other is very flat over the range $-120° \alpha < -70°$ (or, equivalently, $60° < \alpha \leqslant 110°$). The growth rate pattern is found to have two local maxima only when the Richardson number is in the range $0.845 > Ri > 0.82$ (with $Ek = 0.001$). This range is much smaller than the range $1 > Ri > 0.84$ for the coexistence of two local maxima in the inviscid case.

In their figure 6(*a*), Miller & Antar (1986) plotted the growth rate as a function of α at the critical Richardson number ($Ri = 0.926$) and wavelength ($l = 13.2H/L = 13.2/Ro = 0.66$) for the symmetric instability with $Pr = 1.0$, $Ro = 20$ and $Ek = 0.001$. Their growth rate curve showed two peaks on the two sides of $\alpha = 0$ in the range $-8° < \alpha < 8°$ (but the negative growth rates over the range $0 \leqslant \alpha \leqslant 1°$ could not be computed by their time-integration technique). This double-peak distribution indicates that the tilted modes are unstable while the symmetric mode is marginally unstable, so the tilted modes are more unstable than the symmetric mode. The double-peak distribution can be compared with the growth rate distribution along the vertical line of $l = 0.66$ between $-8° \leqslant \alpha \leqslant 8°$ in figure 4(*b*). A detailed comparison (not shown) indicates that the two growth rate distributions have the same shape.

The dashed curve (dotted curve) in figure 5 shows how the conditional maximum growth rate changes from the lower solid curve (for $Ri = 0.92$) when Pr is doubled to 2.0 (halved to 0.5) with the modified Ekman number $Ek/\sqrt{Pr}$ fixed. In the vicinity of $\alpha = 0$, the major change is an up-leftward (down-rightward) shift of the V-shape profile in response to the increase (decrease) of Pr. In comparison with the profiles of the conditional maximum growth rates obtained in figure 10 of Miller & Antar (1986) for $Pr = 2.0$ and 0.5 but with Ek fixed, the above changes are quite small. Thus, the growth rate pattern becomes less dependent on Pr when $Ek/\sqrt{Pr}$ is fixed than when Ek is fixed. This is consistent with the results in § 5.4 for the same reason as given in § 4.4.

6.2. *Comparisons with Stone's inviscid results*

As manifested by the continuous dependence of the growth rate on α, the nearly symmetric and nearly baroclinic instabilities studied in this paper are continuous extensions of the viscous symmetric instability. According to McIntyre (1970), the viscous symmetric instability does not converge to the classic inviscid symmetric instability in the limit of vanishing Ekman number unless $Pr = 1$. The nearly symmetric and nearly baroclinic instabilities are continuous extensions of the viscous symmetric instability, so they must also not converge to the inviscid instabilities studied by Stone (1970) unless $Pr = 1$. This speculation is verified numerically by the solutions of the spectral model used in this paper. In particular, it is found (but not shown here) that the growth rate pattern computed with $Pr = 0.5$ or 2 does not converge to the inviscid results of Stone (1970) as Ek becomes infinitely small. Thus, Pr will be fixed at unity while Ek is further reduced (to 0.0001) for the comparisons with Stone's inviscid results in this section.

When the Ekman number is reduced to 0.0001 from the value of 0.001 in figure 3, the growth rate pattern and associated frequency pattern become almost symmetric with respect to the symmetric axis (see figure 1 of Part 2, Xu 2003). The main growth rate pattern (for the non-propagating modes) remains largely the same as that in figure 3, but the maximum growth rate increases from 0.736 to 0.913 (which is very close to its inviscid limit), the maximum point moves from (0.347, $-0.29°$) to (0.186, $-0.005°$), and the two side lobes (for the propagating modes) become about three times as large as those in figure 3. A similar but slightly more rapid convergence to the inviscid limit is seen for the free-slip case. Because of this, we only need to compare the growth rates obtained with the non-slip boundary conditions with Stone's inviscid results in this section.

The time scale and length scales used in this paper are the same as in Stone (1970), so the results can be compared directly. The growth rates obtained for $Ri = 0.5$ and $Ek = 0.0001$ are plotted in figure 6(a) as functions of $k \sin\alpha$ for different values of $k \cos\alpha$ in the same way as in figure 4 of Stone (1970). The growth rates in figure 6(a) are very close to the inviscid growth rates in figure 4 of Stone (1970), and the differences are nearly imperceptible except for the propagating modes (with $\omega \neq 0$) over the outer range of $|k \sin\alpha| > 2.0$ (see figure 6b). The non-propagating modes (with $\omega = 0$) are mostly in the inner range of $|k \sin\alpha| \leqslant 2$, while the propagating modes are over the outer range of $|k \sin\alpha| > 1$. As defined in (3.3), ω is the frequency relative to the middle-level basic flow. The frequency plotted for $k \cos\alpha = 15$ in figure 6 of Stone (1970) was defined relative to the bottom-level basic flow at $z = 0$, so it corresponds to $0.5k \sin\alpha + \omega$ in this paper. When $0.5k \sin\alpha$ is added to ω in figure 6(b), the frequency curve for $k \cos\alpha = 15$ becomes essentially the same as the inviscid one in figure 6 of Stone (1970).

As the Ekman number increases from $Ek = 0.0001$ to 0.001 (not shown), the growth rate curves (mainly for $k \cos\alpha \geqslant 6$) become slightly flatter than those in figure 6(a). As the Ekman number further increases to 0.005 (figure 7a) and 0.01 (figure 7b), the growth rate curves decrease significantly and become increasingly asymmetric with respect to the point $k \sin\alpha = 0$. The growth rates on the positive side of $k \sin\alpha$ are suppressed by the diffusivity much more severely than on the negative side, especially when $k \cos\alpha$ is large. This must be caused by the difference in the vertical structures between the two modes with opposite signs of $k \sin\alpha$ (see (2.6)–(2.9) of Stone (1970) for the analytical expression for the inviscid vertical velocity). Detailed analyses of the mode structures and related differences will be given in Part 2 (Xu 2003). Note that

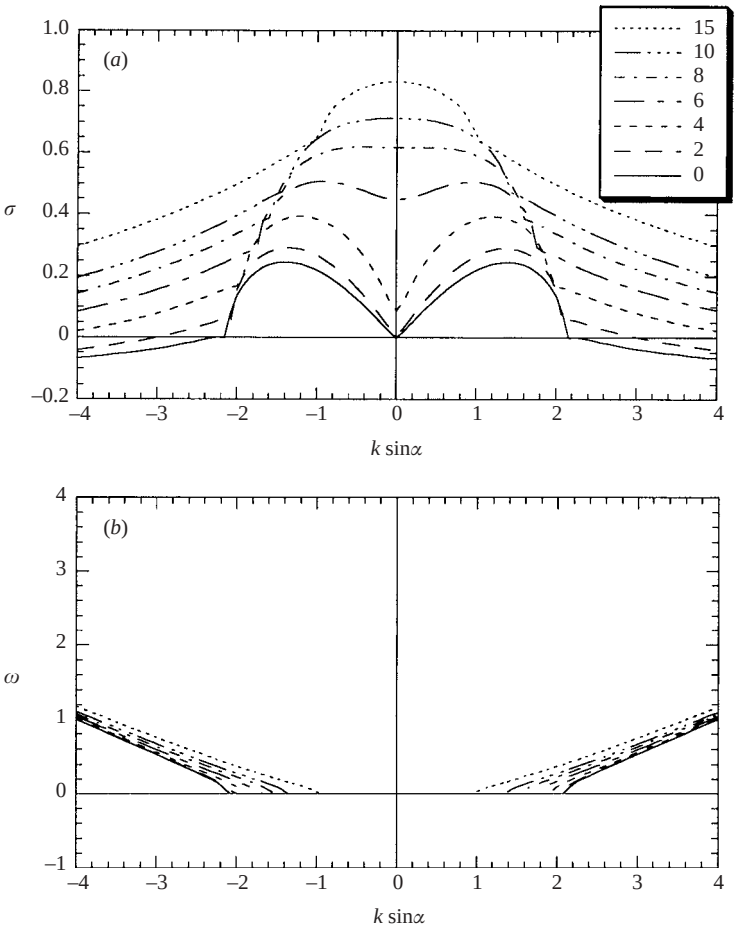

FIGURE 6. Growth rates (a) and frequencies (b) plotted as functions of $k \sin\alpha$ for $k \cos\alpha = 0$, 2, 4, 6, 8, 10 and 15 for the non-slip case. The external parameter values are as in figure 2(a) except that $Ek = 0.0001$. The growth rate curves are plotted in the same way as in figure 4 of Stone (1970) to facilitate comparisons.

the growth rate and frequency curves for $k \cos\alpha = 0$ are always symmetric, as shown in figures 6 and 7, because the positive ($k \sin\alpha > 0$) and negative ($k \sin\alpha < 0$) parts of the baroclinic axis ($k \cos\alpha = 0$) correspond to the two axes defined by $\alpha = 90°$ and $\alpha = -90°$, respectively, in the (l, α) space and these two axes are equivalent as explained earlier.

When the Richardson number increases from $Ri = 0.5$ to 1.0, the growth rates decrease dramatically from those in figure 6(a). As shown in figure 8, the growth rates are very close to the inviscid ones in figure 2 of Stone (1970). In particular, the growth rate curve for $k \cos\alpha = 0$ is very close to that for the classic Eady instability. The above comparisons show that the viscous growth rate patterns (with $Pr = 1$) converge to the inviscid ones obtained by Stone (1970) in the limit of $Ek \to 0$. When Ek is reduced to 0.0001, the unstable modes and growth rates become nearly inviscid.

Nearly inviscid growth rate patterns (with $Ek = 0.0001$) are computed and examined for different values of the Richardson number over the range $1 \geqslant Ri \geqslant 0.25$. The

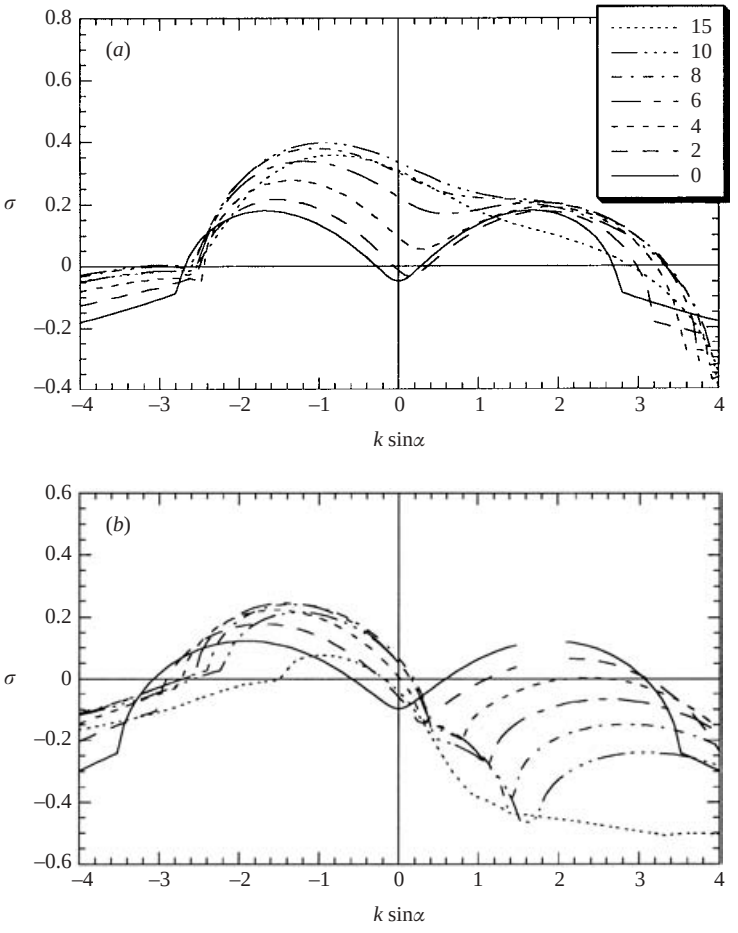

FIGURE 7. (*a*) As in figure 6(*a*) except that $Ek = 0.005$. (*b*) As in (*a*) except that $Ek = 0.01$.

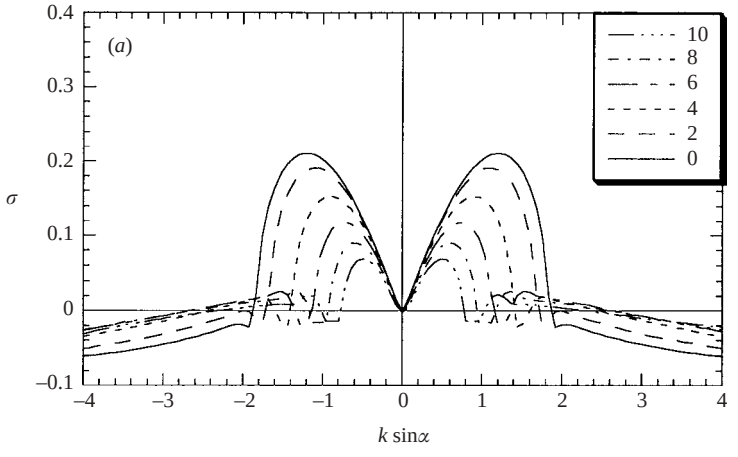

FIGURE 8. Growth rates plotted as functions of $k \sin\alpha$ for $k \cos\alpha = 0$, 2, 4, 6, 8 and 10 for the non-slip case. The external parameter values are as in figure 6 except that $Ri = 1.0$. The growth rate curves are plotted in the same way as in figure 2 of Stone (1970).

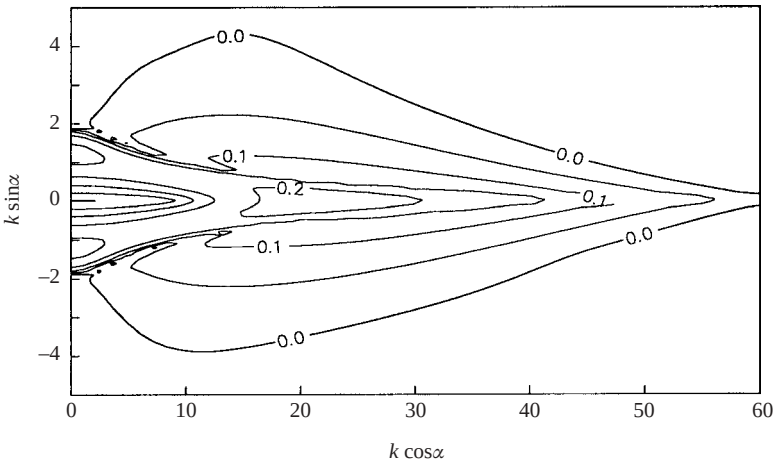

FIGURE 9. Growth rates plotted in the wavenumber space ($k\cos\alpha, k\sin\alpha$) for $\sigma \geqslant 0$ for the non-slip case. The external parameter values are as in figure 2(a) except that $Ek = 0.0001$ and $Ri = Ri^* = 0.913$.

main results can be summarized as follows:

(i) The growth rate pattern has two local maxima when $0.92 > Ri > 0.82$ (note that this range is smaller than $1 > Ri > 0.84$ for the coexistence of two local maxima in the inviscid case). The two local maxima are located very close to (but not exactly on) the symmetric axis ($k\sin\alpha = 0$) and baroclinic axis ($k\cos\alpha = 0$), respectively.

(ii) The largest growth rate is associated with the nearly symmetric mode if $0.913 \geqslant Ri > 0.82$, and with the nearly baroclinic mode if $0.92 > Ri > 0.913$, so the transitional Richardson number is $Ri^* = 0.913$ (for $Ek = 0.0001$ and $Pr = 1$).

(iii) When the Richardson number becomes smaller than 0.82, the local maximum associated with the nearly baroclinic mode degenerates into a saddle point and only one maximum exists in association with a nearly symmetric mode.

(iv) When the Richardson number becomes larger than 0.92, the local maximum associated with the nearly symmetric mode diminishes and only one maximum exists in association with a nearly baroclinic mode.

The nearly inviscid growth rate pattern for $Ri = Ri^* = 0.913$ is plotted in figure 9. As shown, the growth rate pattern has two local maxima with the same growth rate ($\sigma = 0.24$): one is located at ($k\cos\alpha$, $k\sin\alpha$) = (22.8, −0.00014) which is very close to the symmetric axis, while the other is located at ($k\cos\alpha, k\sin\alpha$) = (0.0002, −1.2) which is very close to the baroclinic axis, and the growth rate ($\sigma = 0.24$) is virtually the same as its inviscid limit ($\sigma = 0.24$ at $k = 1.2$ and $\alpha = \pm 90°$). The unstable modes are non-propagating in the main growth rate pattern but become propagating in the two side lobes attached to the concave upper and lower edges of the main growth rate pattern in figure 9. Since all the growth rate patterns are periodic in the α-direction and the period is 180° in the (l, α) space, the growth rate pattern in figure 9 can be extended to the left half-plane of the wavenumber space by a 180°-rotation with respect to the origin.

The maximum growth rate and associated wavelength and tilt angle are plotted as functions of Ri for $Ek = 0.0001$ by the solid curves in figure 10(a–c). In each figure, the solid curve over the range $0.92 \geqslant Ri \geqslant 0.25$ is associated with the nearly symmetric instability, while the solid curve over the range $1 \geqslant Ri \geqslant 0.82$ is associated with the nearly baroclinic instability. The two curves coexist over the range $0.92 \geqslant Ri \geqslant 0.82$

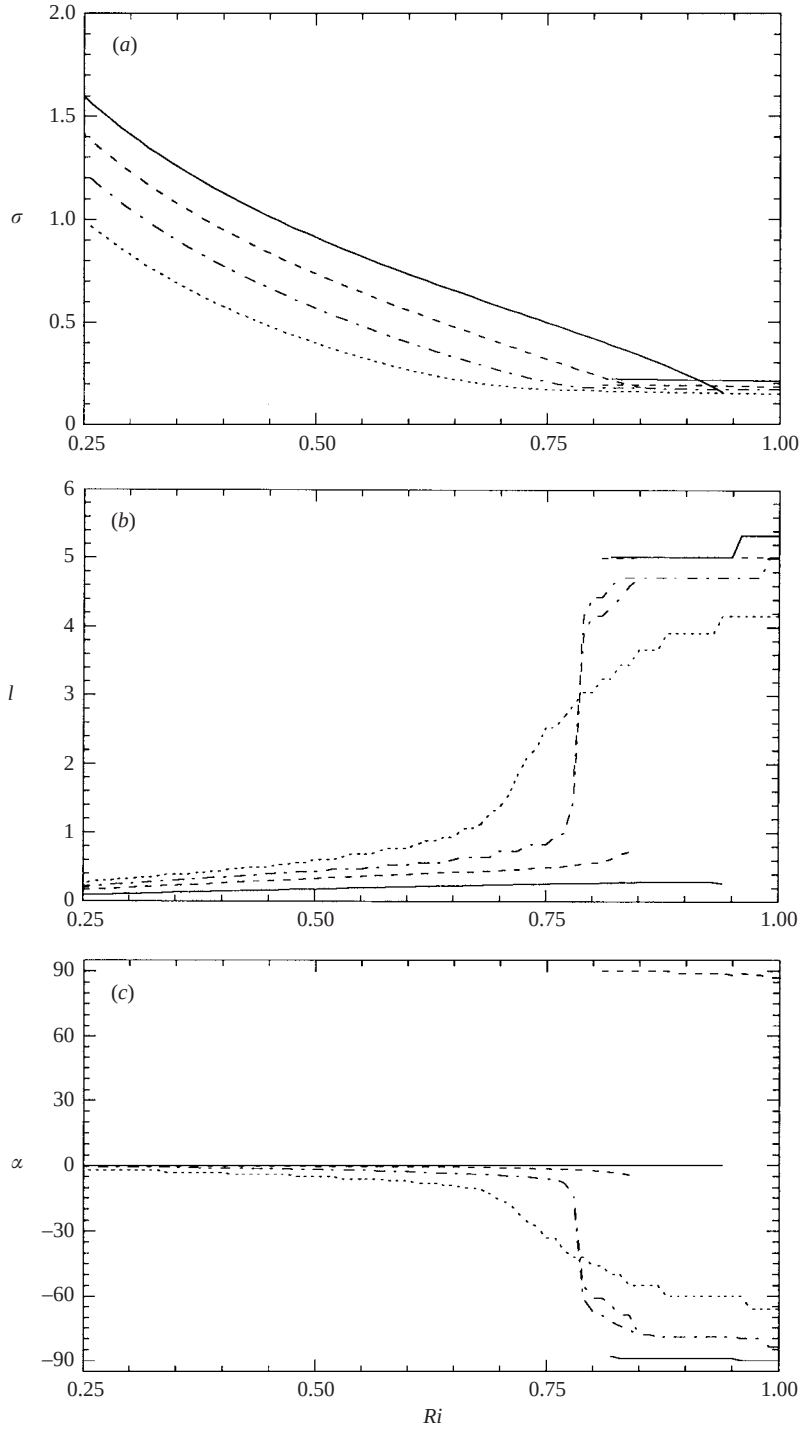

FIGURE 10. Maximum growth rate (a), associated wavelength (b) and tilt angle (c) as functions of Ri for $Ek = 0.0001$ (solid), 0.001 (dashed), 0.0025 (dash-dotted) and 0.005 (dotted) with the non-slip boundary conditions. In (b) and (c), the doubled dash-dotted curves over $0.78 \leqslant Ri \leqslant 0.85$ indicate that the maximum of σ is locally flat in the (l, α) space when $Ek = 0.0025$ and Ri is between 0.78 and 0.85.

and so do the two types of instability. At the transitional Richardson number ($Ri^* = 0.913$), the two local maximum growth rates become equal and thus the two solid curves intersect, as shown in figure 10(a). The two solid curves in figures 10(b) and 10(c) are far apart from each other and their vertical distances apart at $Ri^* = 0.913$ quantify the jump of the global maximum for one local maximum to the other in the (l, α) space. These solid curves are very close to the inviscid limits (not shown but described at the beginning of § 6).

Similar functions are plotted by the dashed curves for $Ek = 0.001$, by the dash-dotted curves for $Ek = 0.0025$, and by the dotted curves for $Ek = 0.005$ in figure 10(a–c). From these curves, we can see how the maximum growth rate and associated wavelength and tilt angle change with Ri and Ek. As Ek increases to 0.0025, the range of Ri for the coexistence of two local maxima diminishes gradually and the transitional Richardson number decrease from $Ri^* = 0.95$ to 0.785.

7. Summary remarks

In this paper, the spectral model of Gu *et al.* (1998) is extended and used to study the instabilities of baroclinically sheared Eady basic flows in three-dimensional space in the presence of diffusivity with two (free-slip and non-slip) types of boundary conditions. The non-dimensional solutions are controlled by four independent external parameters or four non-dimensional combinations of six dimensional external parameters (see (2.6)). The combinations can be selected in different ways which lead to different selections of external parameters. The parameters selected in this paper (see (2.9)) have the merit of reducing the number of the external-control parameters (see §§ 4.2 and 5.2), so the normal-mode solutions are mainly controlled by three external parameters: the Richardson number, the Ekman number and the Prandtl number. The dependence of the growth rate pattern (but not the maximum growth rate) on the Prandtl number may be reduced by fixing the modified Ekman number (defined by $Ek/\sqrt{Pr}$) instead of fixing the Ekman number itself (see §§ 4.4 and 5.4). This modified Ekman number measures the combined effect of μ and κ on the growth rates.

Growth rate patterns are computed for unstable modes as functions of (l, α), where l is the horizontal wavelength and α is the tilt angle of the horizontal orientation of the banded structure of the mode with respect to the basic shear. The growth rate patterns are examined for wide ranges of the three external-control parameters with both (free-slip and non-slip) types of boundary conditions. It is found in general that as long as the Ekman number is not very small, the main growth rate pattern (for non-propagating modes) has only one maximum. When the Richardson number increases from 0.25 to 1.0, the maximum growth rate decreases and the associated instability changes gradually from a nearly symmetric type to a nearly baroclinic type. In this sense, the nearly symmetric and nearly baroclinic instabilities studied in this paper fill the gap between the two classic instabilities: the baroclinic instability and the symmetric instability, ranging from synoptic scale to mesoscale. Clearly, in the presence of moderate diffusivity ($Ek > 0.0025$), the gradual change of instability in response to the continuous increase of the Richardson number is very different from the inviscid results of Stone (1966, 1970).

The growth rate patterns are found to be moderately sensitive to the type of boundary conditions unless the Ekman number is very small. When the Ekman number is very small ($Ek \leqslant 0.001$) and the Richardson number is between 0.25 and the transitional Richardson number ($Ri^* = 0.95$ in the inviscid limit), the growth rate

pattern is characterized in general by a V-shape ridge with two branches split from a main ridge along the two sides of the symmetric axis (figures 3 and 4(a)). As the Ekman number increases (say to $Ek = 0.01$), the main ridge collapses and the global maximum point moves along the negative-α branch while the positive-α branch goes below zero for the non-slip case but not for the free-slip case (figures 1(a) and 2(a)). In general, the growth rate pattern obtained with the free-slip boundary conditions has a slightly larger global maximum and is more symmetric with respect to the symmetric axis than that obtained with the non-slip boundary conditions for any given set of external-control parameter values in the ranges considered in this paper.

The nearly symmetric modes and nearly baroclinic modes are mixed baroclinic–symmetric modes of instability, that could not be represented in the classic models because they did allow them. Their instability mechanisms are largely unexplored, although the energy conversions of nearly symmetric modes with weak diffusivity and weak instability were examined by Miller & Antar (1986). To physically understand and interpret the major changes in the growth rate patterns caused by the presence of diffusivity and major differences caused by the boundary conditions, described above, it is necessary to analyse the mode structures and related energetics, and this will be performed in Part 2 of the study (Xu 2003).

The author is grateful to Drs Wei Gu and Ting Lei for developing the spectral model. The work was partially supported by the NSF Grant ATM-9983077 to the University of Oklahoma. Comments and suggestions from Dr Douglas Lilly and anonymous reviewers improved the presentation of the results.

REFERENCES

Antar, B. N. & Fowlis, W. W. 1983 Three-dimensional baroclinic instability of a Hadley cell. *J. Fluid Mech.* **137**, 425–447.

Browning, K. A., Chapman, D. & Dixon, R. S. 2001 Stacked slantwise convective circulations. *Q. J. R. Met. Soc.* **127**, 2513–2536.

Buizza, R. & Palmer, T. N. 1995 The singular-vector structure of the atmospheric global circulation. *J. Atmos. Sci.* **52**, 1434–1456.

Busse, F. H. & Chen, W. L. 1981 On the (nearly) symmetric instability. *J. Atmos. Sci.* **38**, 877–880.

Chapman, D. & Browning, K. A. 2001 Measurements of dissipation rate in frontal zones. *Q. J. R. Met. Soc.* **127**, 1939–1959.

Eady, E. T. 1949 Long waves and cyclone waves. *Tellus* **1**, 33–52.

Emanuel, K. A. 1979 Inertial instability and mesoscale convective systems. Part I: Linear theory of inertial instability in rotating viscous fluids. *J. Atmos. Sci.* **36**, 2425–2449.

Emanuel, K. A. 1985 Comments on "Inertial Instability and Mesoscale Convective Systems. Part I". *J. Atmos. Sci.* **42**, 747–752.

Farrell, B. F. & Ioannou, P. J. 1996 Generalized stability theory. I. Autonomous operators. *J. Atmos. Sci.* **53**, 2025–2040.

Fjortoft, R. 1944 On the frontogenesis and cyclogenesis in the atmosphere. Part I. On the stability of the stationary circular vortex. *Geofys. Publ.* **16**, No. 5, 1–28.

Gu, W., Xu, Q. & Wu, R. 1998 Three-dimensional instability of nonlinear viscous symmetric circulations. *J. Atmos. Sci.* **55**, 3148–3158.

Jones, S. C. & Thorpe, A. J. 1992 The three-dimensional nature of 'Symmetric' instability. *Q. J. R. Met. Soc.* **118**, 227–258.

Kennedy, P. J. & Shapiro, M. A. 1980 Further encounters with clear air turbulence in research aircraft. *J. Atmos. Sci.* **38**, 986–993.

McIntyre, M. E. 1970 Diffusive destabilization of the baroclinic circular vortex. *Geophys. Fluid Dyn.* **1**, 19–57.

Miller, T. L. & Antar, B. N. 1986 Viscous nongeostrophic baroclinic instability. *J. Atmos. Sci.* **43**, 329–338.

Pepler, S. J., Vaughan, G. & Hooper, D. A. 1998 Detection of turbulence around jet streams using a VHF radar. *Q. J. R. Met. Soc.* **124**, 447–462.

Stone, P. H. 1966 On non-geostrophic baroclinic stability. *J. Atmos. Sci.* **23**, 390–400.

Stone, P. H. 1970 On non-geostrophic baroclinic stability: Part II. *J. Atmos. Sci.* **27**, 721–726.

Stone, P. H. 1972 On non-geostrophic baroclinic stability: Part III. The momentum and heat transports. *J. Atmos. Sci.* **29**, 419–426.

Tokioka, T. 1970 Nongeostrophic and non-hydrostatic stability of a baroclinic fluid. *J. Met. Soc. Japan* **48**, 503–520.

Xu, Q. 1987 The existence and stability of steady circulations in a conditionally symmetrically unstable basic flow. *J. Atmos. Sci.* **44**, 3020–3029.

Xu, Q. 1988 A formula for eddy viscosity in the presence of moist symmetricinstability. *J. Atmos. Sci.* **45**, 5–8.

Xu, Q. 2003 Nearly symmetric and nearly baroclinic instabilities in the presence of diffusivity. Part 2. Mode structures and energetics. *J. Fluid Mech.* (accepted).